Numerical Modeling of Bubbly Flow in Continuous Casting Mold using Two Population Balance Approaches

Zhongqiu Liu[a,b], Alexander Vakhrushev[b], Menghuai Wu[b], Andreas Ludwig[b], Baokuan Li[a], Guodong Xu[c]

a. School of Metallurgy, Northeastern University, Shenyang, 110819, China
b. Christian Doppler Laboratory for Advanced Process Simulation of Solidification and Melting, University of Leoben, Austria
c. Baowu Steel Group Corporation Limited, Shanghai, ,China

ABSTRACT: *To model the spatial evolution of the gas bubbles in continuous casting mold, two population balance approaches of MUlti-SIze-Group (MUSIG) model and Average Bubble Number Density (ABND) model, -have been employed and merged with the Euler-Euler two-fluid model. The bubble induced turbulence model and various interfacial forces including drag, lift, virtual mass, and turbulent dispersion are incorporated in both of models. A 1/4th scaled water model was built to measure and investigate the bubble behavior and size distribution in the mold. Predictions by MUSIG model and ABND model were in reasonable agreement with experimental data of gas void fraction, liquid flow pattern, and local bubble size distribution profiles. The "intermediate peak" and "core peak" behaviors of void fraction inside the submersed entry nozzle (SEN) had been captured very well. From a practical perspective, the ABND model may be considered as a more viable approach for industrial applications of gas-liquid two-phase flow systems.*

KEYWORDS: *Bubble size distribution, MUSIG model, ABND model, continuous casting mold*

INTRODUCTION

In continuous casting process, argon gas is injected into the submerged entry nozzle (SEN) to prevent the nozzle clogging, and to remove non-metallic inclusions. The flow regimes found in continuous casting mold show a spectrum of different bubble sizes.[1-5] Large bubbles rise toward the top surface due to buoyancy and are subsequently removed from the mold, while small bubbles are carried deep into the liquid pool. However, fine argon bubbles were sometimes observed inside the continuous casting slabs, which were trapped by the solidified shell.[6-8] In the subsequent rolling process, these bubbles can lead to the formation of pinhole defects. A schematic of bubbly flow in the continuous casting mold was shown in Fig.1. To better optimize continuous casting process, a greater reliance on the fundamental knowledge of bubble size distribution (BSD) is required.

Although some of water model studies have reported the BSD in the SEN[9,10] or mold[3-5] after air injected through the SEN, few computational models have been actively developed for studying the complex polydispersed bubbly flow in the mold. However, most previous attempts utilized an assumed mean bubble size for the simulations of the dispersed gas-liquid flow; but not the local BSD. This assumed size was often adjusted based on attempts to match model predictions to some measured result. Moreover, the fluid flow pattern and gas void fraction were not always predicted well by assumption of the constant bubble size.

In order to predict the BSD, the population balance equation(PBE) need to be calculated. Several numerical techniques for solving the PBE have been proposed: the Monte Carlo method,[11] the discrete class method,[12] the quadrature method of moments,[13] and the least square method.[14] Among these available techniques, the discrete class method has received particular interest due to its rather straightforward implementation within CFD program. Two kind of discrete class methods are therefore adopted in the present work. The Multiple Size Group (MUSIG) model.[2,5,15,16] has been developed to deal with polydispersed multiphase flows in which the dispersed phase features a large variation in its characteristic sizes. This approach provides a framework in which the population balance model (PBM) can be incorporated into three-dimensional calculations. Modelling of two-phase flow in the mold using this approach match well with measurements of both flow pattern and bubble size in water models, except near to the SEN. [5,15,16] But a series of additional equations have to be solved to accommodate the range of bubble sizes and its population changes caused by coalescence and breakage of bubbles. Excessive computational calculations are needed to solve a large number of bubble classes for bubbly flow. Recently,

an average bubble number density (ABND) equation was developed by Cheung et al.[17] to calculate the vertical bubbly flow. The population balance of bubbles is attuned by the equation source terms describing the temporal and spatial coalescence and breakage mechanisms. Then Liu et al.[18] studied the polydispersed bubbly flow in the slab continuous casting mold using this approach, comparisons of gas void fraction, liquid flow pattern, and local bubble size distribution profiles with experimental measurements are provided, showing the applicability and accuracy of the ABND approach in modeling the polydispersed bubbly flow in the mold.

Based on our previous work, the primary aim of this paper is to determine the relative merits and capabilities applying two population balance approaches (i.e., MUSIG and ABND models) within the CFD framework to resolve the polydispersed bubbly flow in the slab continuous casting mold. Predictions by the ABND and MUSIG models are compared against our previous experimental data.
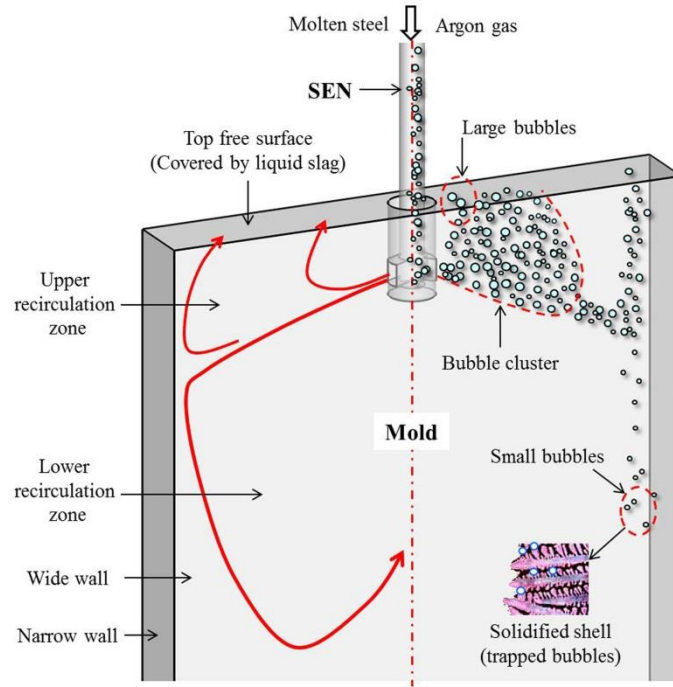
Fig.1 - Schematic of bubbly flow in the continuous casting mold

MATHEMATICAL MODELS
Euler-Euler Two-fluid model
The mathematical model presented in the present work is based on the Euler-Euler two-fluid model.[19-21] The continuity and momentum equations of the two phases can be written as:

$$\frac{\partial(\rho_h \alpha_h)}{\partial t} + \nabla \cdot \left(\alpha_h \rho_h \mathbf{u}_h \right) = 0 \tag{1}$$

$$\frac{\partial(\rho_h \alpha_h \mathbf{u}_h)}{\partial t} + \nabla \cdot \left(\alpha_h \rho_h \mathbf{u}_h \mathbf{u}_h \right) = -\alpha_h \nabla P + \alpha_h \rho_h \mathbf{g} - \nabla \cdot \left[\alpha_h (\mu_{T,h} + \mu_{BI,h})(\mathbf{u}_h + \mathbf{u}_h^{\mathrm{T}}) \right] + F_h \tag{2}$$

The subscripts $h = l$ or g denotes the liquid or gas phase.

The model proposed by Sato et al. [22] has been used to take account of the turbulence induced by the movement of the bubbles. The expression is:

$$\mu_{BI,l} = \rho_l C_{\mu,BI} \alpha_g D_S \left| \mathbf{u}_g - \mathbf{u}_l \right| \tag{3}$$

Shear Stress Transport model
The turbulence viscosity is calculated using the Shear Stress Transport (SST) model:

$$\mu_{T,l} = \frac{\rho \alpha_l k}{\max\left(\alpha_l \omega, SF_1\right)} \tag{4}$$

The ensemble-averaged transport equations of the SST model are given as:

$$\frac{\partial \rho_l \alpha_l k}{\partial t} + \nabla \cdot (\alpha_l \rho_l \mathbf{u}_l k) = \nabla \cdot \left(\alpha_l \frac{\mu_{T,l}}{\sigma_{k,SST}} \nabla k \right) + \alpha_l P_k - \rho_l \beta_{SST} k\omega \tag{5}$$

$$\frac{\partial \rho_l \alpha_l \omega}{\partial t} + \nabla \cdot (\alpha_l \rho_l \mathbf{u}_l \omega) = \nabla \cdot \left(\alpha_l \frac{\mu_{T,l}}{\sigma_{\omega,SST}} \nabla \omega \right) - 2\rho_l \alpha_l (1 - F_2) \frac{1}{\sigma_{\omega,SST}\omega} \frac{\partial k}{\partial x_j} \frac{\partial \omega}{\partial x_j} + \alpha_l \gamma \frac{\omega}{k} P_k - \rho_l \beta_{SST} \tag{6}$$

Interfacial Momentum Transfer

Interfacial momentum transfer exhibits a dominant effect in the multi-phase momentum equations. The interfacial force between the two phases is given as follows:

$$F_h = F_{lg} = -F_{gl} = F_{lg}^D + F_{lg}^L + F_{lg}^{VM} + F_{lg}^{TD} \tag{7}$$

The terms on the right hand side are respectively drag, lift, virtual mass, and turbulent dispersion force. A brief description of each interfacial force component is presented below.

$$F_{lg}^D = \frac{1}{8} C_D \alpha_{IAC} \rho_l |\mathbf{u}_g - \mathbf{u}_l| (\mathbf{u}_g - \mathbf{u}_l) \tag{8}$$

$$F_{lg}^L = \alpha_g \rho_l C_L (\mathbf{u}_g - \mathbf{u}_l) \times (\nabla \times \mathbf{u}_l) \tag{9}$$

$$F_{lg}^{VM} = \alpha_g \rho_l C_{VM} \left(\frac{D\mathbf{u}_g}{Dt} - \frac{D\mathbf{u}_l}{Dt} \right) \tag{10}$$

$$F_{lg}^{TD} = C_{TD} C_D \frac{\upsilon_{t,g}}{\sigma_{t,g}} \left(\frac{\nabla \alpha_l}{\alpha_l} - \frac{\nabla \alpha_g}{\alpha_g} \right) \tag{11}$$

where C_D is the drag force coefficient. C_L is the lift force coefficient. C_{VM} is the virtual mass force coefficient. C_{TD} is the turbulent dispersion coefficient.

MUSIG model

The MUSIG model employs multiple discrete bubble size groups to represent the population balance of bubbles. The individual number density of bubble group-*i* can be expressed as:

$$\frac{\partial n_i}{\partial t} + \nabla \cdot (\vec{u}_g n_i) = B_C + B_B - D_C - D_B \tag{12}$$

where n_i is the number density of group-*i* bubbles. B_B, D_B, B_C and D_C respectively represent the birth rate due to breakup of larger bubbles, the death rate due to breakup into smaller bubbles, the birth rate due to coalescence of smaller bubbles, and the death rate due to coalescence with other bubbles.

The birth and death rates of bubbles due to turbulence induced breakage are formulated as:

$$B_B = \sum_{j=i+1}^{N} \Omega(v_j : v_i) n_j \tag{13}$$

$$D_B = \Omega_i n_i \tag{14}$$

The breakup rate of volume v_j into v_i is modeled according to the Luo and Svendsen model.[23]

$$\Omega(v_j : v_i) = 0.923 F_B (1 - \alpha_g) n_j \left(\frac{\varepsilon}{d_j^2} \right)^{1/3} \int_{\xi_{min}}^{1} \frac{(1+\xi)^2}{\xi^{11/3}} \exp\left(-\frac{12(f_{BV}^{2/3} + (1 - f_{BV}^{2/3}) - 1)\sigma}{2\rho_l \varepsilon^{2/3} d_j^{5/3} \xi^{11/3}} \right) d\xi \tag{15}$$

where F_B is the breakage calibration factor.

The birth and death rates of bubbles due to turbulence collision induced coalescence are formulated as:

$$B_C = \frac{1}{2} \sum_{j=1}^{i} \sum_{k=1}^{i} \eta_{jki} \chi_{ij} n_i n_j \tag{16}$$

$$D_C = \sum_{j=1}^{N} \chi_{ij} n_i n_j \tag{17}$$

The coalescence rate considering turbulence collision taken from Prince and Blanch model[24] can be expressed as:

$$\chi_{ij} = F_C \frac{\pi}{4} \left[d_i + d_j \right]^2 (\vec{u}_{ti}^2 + \vec{u}_{tj}^2)^{0.5} \exp\left(-\frac{t_{ij}}{\tau_{ij}} \right) \tag{18}$$

where F_C is the coalescence calibration factor.

ABND model

The population balance of dispersed bubbles is mainly governed by three mechanisms of bubble coalescence and breakage, which can be expressed in the following ABND transport equation:

$$\frac{\partial n}{\partial t} + \nabla \cdot \left(\mathbf{u}_g n \right) = \varphi_n^{RC} + \varphi_n^{TI} + \varphi_n^{WE} \tag{19}$$

where n is the average bubble number density. ϕ_n^{RC}, ϕ_n^{TI}, and ϕ_n^{WE} are the bubble number density changes due to random collision, turbulent induced breakage and wake entrainment.

The bubble number density for bubbly flow can be defined as:

$$n = \frac{\alpha_g}{\pi D_S^3 / 6} = \frac{1}{36\pi} \cdot \frac{\alpha_{IAC}^3}{\alpha_g^2} \tag{20}$$

The phenomenological mechanism of coalescence and breakage source terms need closure to describe the spatial evolution of the gas phase. An empirical modeling of the source and sink terms for bubble coalescence and breakage was developed by Wu et al.[25] For bubble coalescence, two mechanisms were considered: the random collisions between bubbles due to turbulence and the wake entrainment process due to the relative motion of the bubbles in the wake region of a seeding bubble. Considering the characteristic times for binary collision and the mean travelling length between neighboring bubbles, they have modeled the random collision rate of bubble coalescence according to:

$$\phi_n^{RC} = -C_{RC} \frac{\alpha_g^2 \varepsilon^{1/3}}{D_S^{11/3} \alpha_{\max} (\alpha_{\max}^{1/3} - \alpha_g^{1/3})} \left[1 - \exp\left(-\frac{C \alpha_{\max}^{1/3} \alpha_g^{1/3}}{\alpha_{\max}^{1/3} - \alpha_g^{1/3}} \right) \right] \tag{21}$$

Assuming a spherical bubble travelling with its terminal velocity, the rate of collision caused by wake entrainment is expressed as:

$$\phi_n^{WE} = -\frac{C_{WE} U_t \alpha_g^2}{D_S^4} \tag{22}$$

For bubble breakage, the impact of turbulent eddies was included. The breakage rate of bubbles is given by

$$\phi_n^{TI} = C_{TI} \frac{\alpha_g \varepsilon^{1/3}}{D_S^{11/3}} \left(1 - \frac{We_{cr}}{We} \right) \exp\left(\frac{We_{cr}}{We} \right) \tag{23}$$

NUMERICAL DETAILS

Numerical simulations are achieved through using of the generic computational fluid dynamic (CFD) code ANSYS-CFX-15.0. Ten bubble groups were specified for the dispersed phases in the MUSIG model. By modeling the fundamental mechanisms of bubble breakup and coalescence, population change of each group and the overall BSD evolution are explicitly resolved as source terms within the transport equations. The ABND equation and different source terms describing the coalescence and breakage of bubbles are implemented through the CFX Command Language (CCL). The pressure-velocity coupling was obtained using the SIMPLEC algorithm. The third-order QUICK scheme was used for all the convection terms.

A mass flow boundary was set at the water inlet of the SEN based on the casting speed. A mass flow boundary was set at the air inlet of the SEN, because the diameters of the injected bubbles were unknown,

uniformly distributed bubble size was specified in accordance with the flow conditions, and all bubbles enter into the SEN with an initial bubble diameter of 1mm. A constant pressure outlet condition at the bottom of the calculation domain is applied. The top surface of the mold cavity is modeled as degassing boundary condition, where dispersed bubbles are permitted to escape, but the liquid is not. Along the walls, no-slip boundary condition is adopted. More details can be seen in previous works. [5,15,16,18]
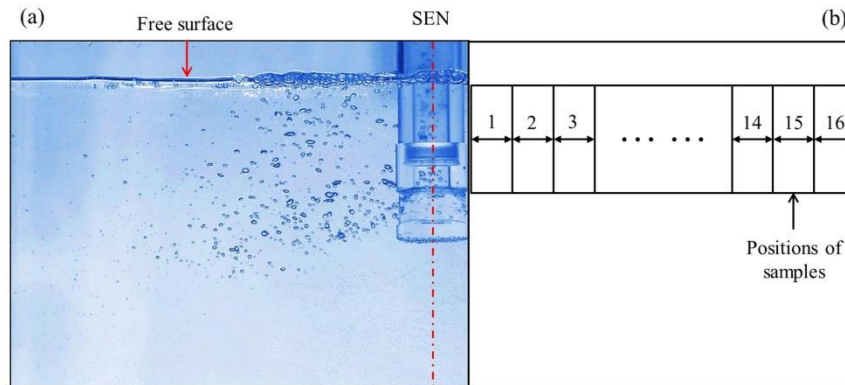
Fig.2 - Transient bubble distribution in water model (a) and schematic of calculating the bubble mean diameter (b)

RESULTS AND DISCUSSION
Gas Void Fraction Distribution

Figure 2(a) shows a close-up photograph of transient bubble distribution inside the mold obtained by a high-speed camera with 1000 frames per second and a laser light-sheet. The polydispersed bubbly flow can be clearly seen from this figure. In order to study the BSD along the width of the mold, the region of interest in the upper recirculation zone was divided into sixteen equal zones. The zone-1 is adjacent to the SEN and the zone-16 is close to the narrow wall of the mold, as shown in Fig. 2(b). Then the population and mean sizes of bubbles of each zone were measured through the image analysis software of ImageJ. Three different water flow rates and gas flow rates were employed in the present study.
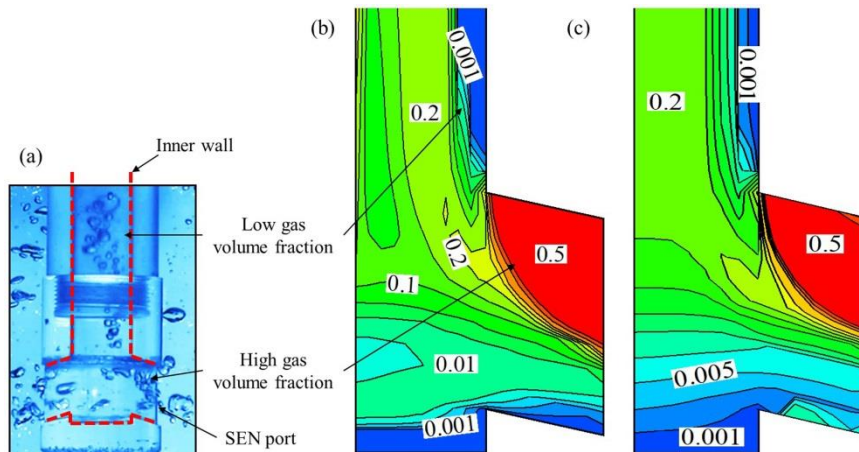
Fig.3 - Gas void fraction profiles inside the SEN obtained from the MUSIG model (a) and ABND model (b)

Figure 3(a) shows a close-up photograph of transient bubble distribution inside the SEN. It is observed that a well-developed "intermediate peak" behavior of void fraction was recorded in the experiment. Most of bubbles were transported around the center of the SEN. Few bubbles or low gas void fractions were found near the side wall and the bottom of the SEN. At the upper zone of SEN port, a typical "core peak" behavior of void fraction was observed. In the process of experiment, it can be seen that many polydispersed small bubbles with different sizes would gather in this position, and then form larger bubbles through coalescence. Finally, these large bubbles gradually separate themselves from the SEN port and float to the top surface near the SEN. Figure 3(b) and (c) shows the void fraction distribution inside the SEN obtained respectively

from the MUSIG and ABND model. From the result, it is observed that the "intermediate peak" and "core peak" behaviors of void fraction had been captured very well by both of models.
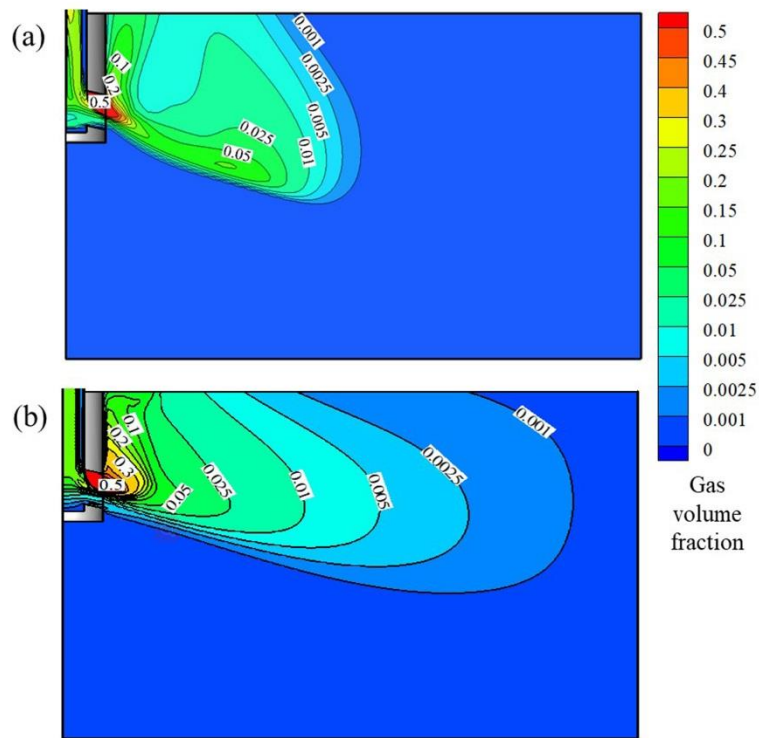
Fig.4 - Gas void fraction profiles in the mold obtained from the MUSIG model (a) and ABND model (b)
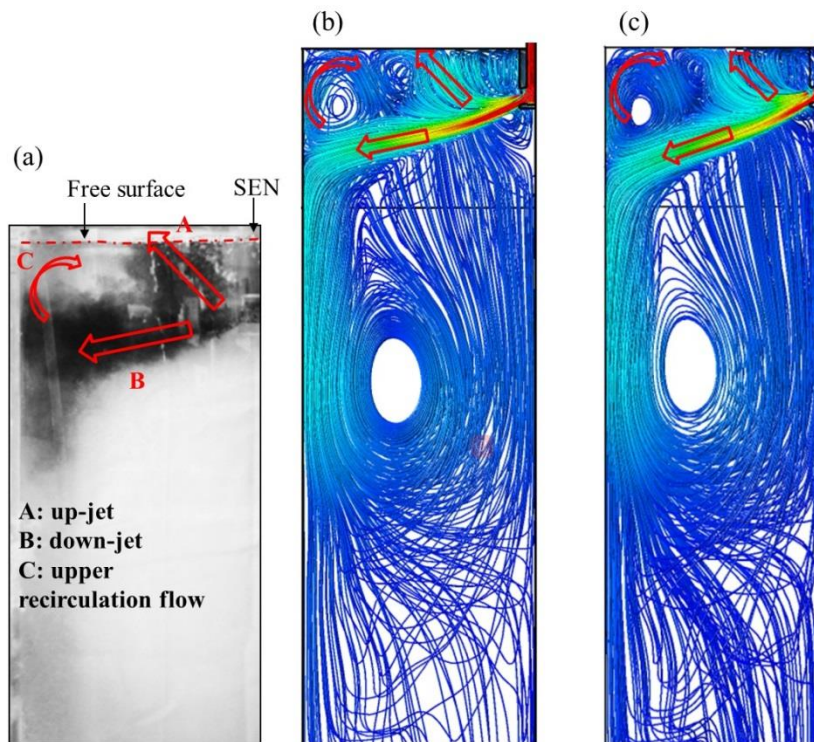
Fig.5 - Liquid flow patterns obtained from the experiment (a), MUSIG model (b) and ABND model (c)

Figure 4 shows the gas void fraction profiles obtained respectively from the MUSIG model and ABND model in the upper recirculation zone with a water flow rate of 21 L/min and a gas flow rate of 1.6 L/min,

corresponding to the bubble dispersion profile in Fig. 2(a). The fan-shaped gas void fraction distribution have been predicted by both of the models, which is similar with the water model experiment result. After entering the mold with the water jet, most of the bubbles are crowded together close to the SEN and float upward through the upper recirculation zone, and then escape from the top surface. Maximum void fraction located at the upper zone of SEN port which is mainly due to the low-pressure in this part. Due to the positive lift force, the small bubbles are pushed toward to the narrow wall and some of them are taken deeper into mold cavity, this phenomenon can be predicted by the current ABND nodel, as shown in Fig. 4(b).

Liquid Flow Pattern

Gas injection affects the casting process in part through its influence on the liquid flow pattern. The extent of this effect depends on both the gas flow rate and the bubble size. The influence of the gas injection on the fluid flow pattern can be seen in Fig. 5(a); it can be seen that part of fluid (up-jet) moved up toward the top surface after leaving the SEN port, another part of fluid continues as a down-jet impinge at a slightly higher location on the narrow wall, and then forming a recirculation flow after the down-jet impinge on the narrow wall. Figure 5(b) and (c) shows the flow pattern in the mold obtained respectively from the MUSIG model and ABND model. It can be seen that both of the flow patterns in the upper recirculation zone are similar to the flow pattern observed in the water model experiment. Part of the jet flows upward to the top surface when exiting the SEN port, another part of fluid continues as a jet impinge on the narrow wall, and then forms a recirculation flow.
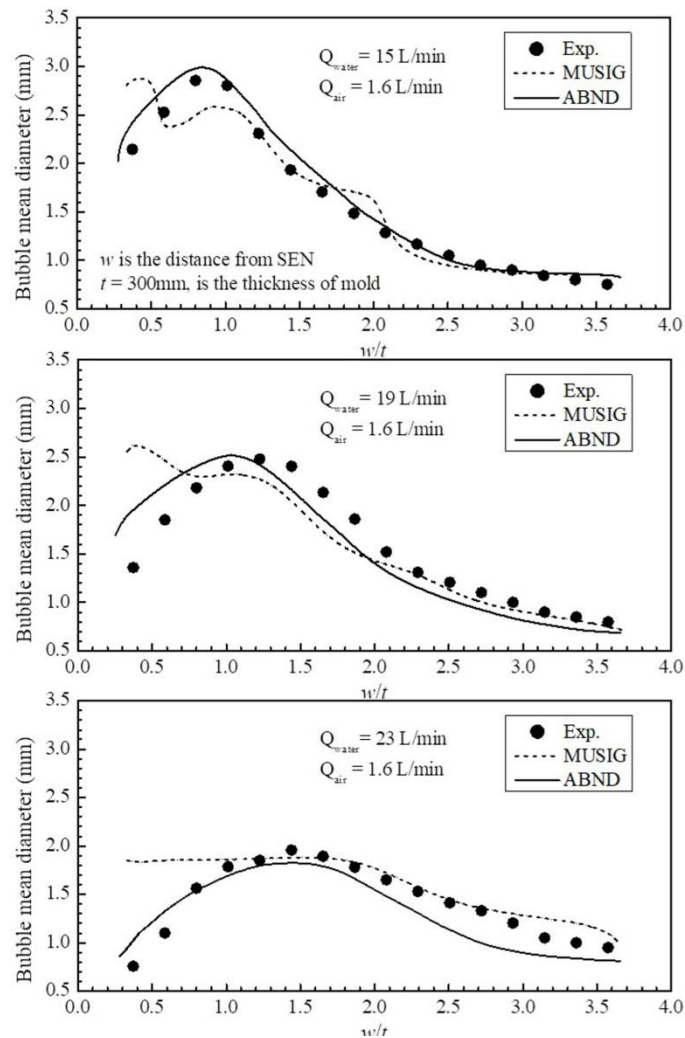
Fig.6 - Predicted bubble Sauter mean diameter distribution and experimental data with different water flow rates of (a) 15 L/min, (b) 19 L/min, (c) 23 L/min
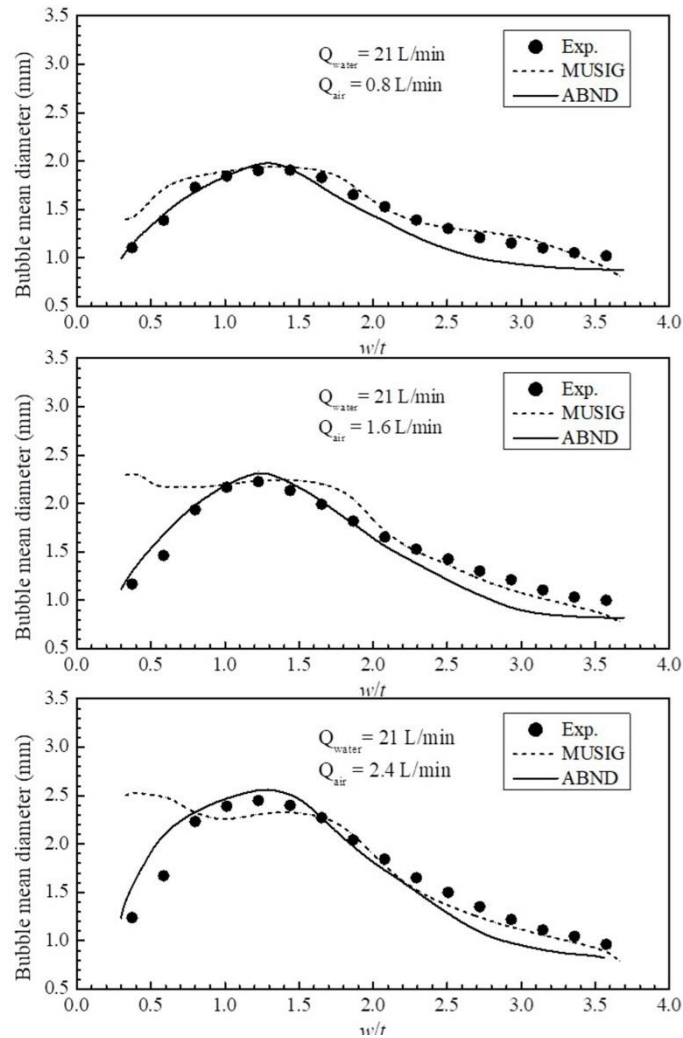
Fig.7 - Predicted bubble Sauter mean diameter distribution and experimental data with different gas flow rates of (a) 0.8 L/min, (b) 1.6 L/min, (c) 2.4 L/min

Bubble Sauter Mean Diameter

Figure 6 (a) to (c) illustrates the predicted and measured bubble Sauter mean diameter distributions at a constant gas injection rate (1.6L/min) with different water flow rates (15, 19 and 21L/min) along the centerline at 25mm below the top surface. From all the results, it is observed that a wide range distribution of bubble Sauter mean diameter was found on the side near the SEN. Both the results of MUSIG and ABND show an agreement between predicted bubble Sauter mean diameters and measured sizes, both qualitatively and quantitatively. Larger bubbles are formed near the SEN where highly concentrated bubbles are having greater possibility to coalescence forming bigger bubbles. Smaller bubbles are migrating toward the narrow wall of the mold. Figure 7 (a) to (c) illustrates the predicted and measured bubble mean diameter distributions at a constant water flow rate (21L/min) with different gas flow rates (0.8, 1.6 and 2.4L/min) along the centerline at 25mm below the top surface. In the upper recirculation zone, with increasing the gas flow rate, a large amount of bubbles stay together and result in a high gas holdup, consequently, coalescence of bubbles takes place in this region and generates larger bubbles. As a result, the peak value of bubble Sauter mean diameter becomes larger, but the locations of peak values do not change significantly. The MUSIG model tends to predict larger bubble Sauter mean diameter closer to the SEN than the experimental measurements. This discrepancy could be attributed to the uncertainties within the MUSIG model in specifically evaluating the coalescence and breakup mechanism as only the turbulence random collision induced coalescence and turbulence vortex induced breakage are considered in the present work. From all the results, it is observed that the ABND model can well predict the bubble mean diameter distribution profiles at various conditions and were in satisfactory agreement with measurements. Since the bubble Sauter mean diameter is generally closely coupled with the turbulent dissipation rate and interfacial

momentum forces, better predictions of the bubble diameter could significantly improve the prediction of the two-phase flow in the mold.

CONCLUSIONS

Euler-Euler two-fluid model coupled with PBM for the polydispersed bubbly flow in a slab continuous-casting mold is demonstrated through the implementations of the MUSIG model and ABND model. For MUSIG model, the Luo and Svendsen model and the Prince and Blanch model are respectively used to calculate the breakage and the coalescence of bubbles. For ABND model, the coalescence of bubbles is formulated according to the random collision driven by turbulence and wake entrainment, and the breakage of bubbles is formulated through considering the impact of turbulent eddies.

Close agreements for both of models were achieved for the void fraction, liquid flow pattern, and bubble Sauter mean diameter against measurements. The "intermediate peak" and "core peak" behaviors of void fraction inside the SEN had been captured very well. Finally, the MUSIG model tends to predict larger bubble Sauter mean diameter closer to the SEN than the experimental measurements. The ABND model thus can be considered as a viable option for a tool in simulating the polydispersed bubbly flow in continuous casting mold with reasonable accuracy and less computation.

REFERENCES

1.   Iguchi M, Kashi N. Water model study of horizontal molten steel-Ar two-phase jet in a continuous casting mold. Metal. Mater. Trans. B. 2000, 31(6): 453-460.
2.   Yuan Q, Shi T, Vanka SP, Thomas BG. In computational modeling of materials, minerals and metals processing, TMS, Warrendale, PA, USA, 2001, P. 491.
3.   Ramos-Banderas A, Morales RD, Sanchez-Perez R, Garcia-Demedices L, and Solorio-Diaz G. Dynamics of two-phase downwards flows in submerged entry nozzles and influence on the two-phase flow in the mold. Int. J. Multiphase Flow 2005, 31: 643-665.
4.   Kwon Y, Zhang J, Lee HG. Water model and CFD studies of bubble dispersion and inclusions removal in continuous casting mold of steel. ISIJ Int. 2006, 46(2): 257-266.
5.   Liu ZQ, Qi FS, Li BK, Cheung SCP. Modeling of bubble behaviors and size distribution in a slab continuous casting mold. Int. J. Multiphase Flow 2016, 79: 190-201.
6.   Liu ZQ, Li BK, Jiang MF. Transient asymmetric flow and bubble transport inside a slab continuous casting mold. Metal. Mater. Trans. B. 2014, 45(4): 675-697.
7.   Liu ZQ, Li BK, Zhang L, Xu GD. Analysis of transient transport and entrapment of particle in continuous casting mold. ISIJ Int. 2014, 54(10): 2324-2333.
8.   Liu ZQ, Li BK. Transient motion of inclusion cluster in vertical-bending continuous casting caster considering heat transfer and solidification. Powder Technology 2016, 287: 315-329.
9.   Bai H, Thomas BG. Bubble formation during horizontal gas injection into downward flowing liquid. Metal. Mater. Trans. B. 2001, 32(12): 1143-1159.
10.   Lee GG, Thomas BG, Kim SH. Effect of refractory properties on initial bubble formation in continuous-casting nozzle. Metall. Mater. Int. 2010,16(3): 501-506.
11.   Ramkrishna D. Population Balance. Academic Press, San Diego, 2000.
12.   Kumar S, Ramkrishna D. On the solution of population balance equations by discretisation -I. A fixed pivot technique. Chemical Engineering Science, 1996, 51: 1311-1332.
13.   Marchisio DL, Pikturna JT, Fox RO, Vigil RD. Quadrature method for moments for population balance equations. A.I.Ch.E. Journal, 2003, 49: 1266-1276.
14.   Dorao CA, Jakobsen HA. A least squares method for the solution of population balance problems. Computer and Chemical Engineering, 2006, 30: 535–547.
15.   Liu ZQ, Li LM, Qi FS, Li BK, Jiang MF, Tsukihashi F. Population balance modeling of polydispersed

bubbly flow in continuous-casting using MUltiple-SIze-Group approach. Metall. Mater. Trans. B. 2015, 46(1): 406-420.

16. Liu ZQ, Qi FS, Li BK, Jiang MF. Multiple Size Group Modeling of polydispersed bubbly flow in the mold an analysis of turbulence and interfacial force models. Metall. Mater. Trans. B. 2015, 46(2): 933-952.

17. Cheung SCP, Yeoh GH, Tu JY. On the modelling of population balance in isothermal vertical bubbly flows-average bubble number density approach. Chem. Eng. Process. 2007, 46: 742-756.

18. Liu ZQ, Li BK, Qi FS, Cheung SCP. Population Balance Modeling of Polydispersed Bubbly Flow in Continuous Casting using Average Bubble Number Density Approach. Powder Technology, 2017, 319: 139-147.

19. Liu ZQ, Li BK, Jiang MF, Tsukihashi F. Modeling of transient two-phase flow in a continuous casting mold using Euler-Euler large eddy simulation scheme. ISIJ Int. 2013, 53(3): 484-492.

20. Liu ZQ, Li BK, Jiang MF, Tsukihashi F. Euler Euler Lagrangian modeling for two phase flow and particle transport in continuous casting mold. ISIJ Int. 2014, 54(10): 1314-1323.

21. Liu ZQ, Li BK. Scale-adaptive analysis of Euler-Euler large eddy simulation for laboratory scale dispersed bubbly flows. Chemical Engineering Journal, 2018, 338: 465-477.

22. Sato Y, Sadatomi M, Sekiguchi K, Momentum and heat transfer in two-phase bubbly flow. Int. J. Multiphase Flow 1975, 2: 79-87.

23. Luo H, Svendsen H. Theoretical model for drop and bubble breakup in turbulent dispersions. A.I.Ch.E. Journal 1996, 42: 1225-1233.

24. Prince MJ, Blanch HW. Bubble coalescence and breakup in air sparged bubble columns. A.I.Ch.E. Journal 1990, 36: 1485-1499.

25. Wu Q, Kim S, Ishii M, Beus SG. One-group interfacial area transport in vertical bubbly flow. Int. J. Heat Mass Trans 1998, 41: 1103-1112.